




Interplay of doping-induced itinerancy and orbital hybridization and their influence on the magnetic and transport properties of $(Y_{1-x}Ca_x)_2Ru_2O_7$

Soumyakanta Panda ¹, Amit Chauhan ^{2,3,*}, B. R. K. Nanda,^{2,3} and N. Mohapatra ^{1,†}

¹*School of Basic Sciences, Indian Institute of Technology Bhubaneswar, Bhubaneswar, Odisha 752050, India*

²*Condensed Matter Theory and Computational Lab, Department of Physics, Indian Institute of Technology Madras, Chennai 600036, India*

³*Center for Atomistic Modelling and Materials Design, Indian Institute of Technology Madras, Chennai 600036, India*



(Received 7 December 2023; revised 18 March 2024; accepted 17 April 2024; published 10 May 2024)

Ruthenium-based pyrochlore oxides exemplify a unique material system in which the competition of Mottness (U), Hundness (J_H), and effective $p-d$ hybridization brings exotic physical characteristics. To understand and manipulate these interactions, we have investigated the structural, magnetic, and electrical properties of the pyrochlore ruthenate $Y_2Ru_2O_7$ and its doped variants $(Y_{1-x}Ca_x)_2Ru_2O_7$. The results of our magnetic measurements reveal a systematic suppression of antiferromagnetic (AFM) ordering and increased frustration with the progressive substitution of Ca at the Y site leading to a nonequilibrium glassy magnetic state at low temperature above the doping level of 10%. Moreover, the screening of the net effective moment of Ru in the doped samples, as derived from the experimental results, is attributed to the induced itinerant character of Ru^{5+} . Such an effect is also reflected in the substantially reduced electrical resistivity, possibly due to enhanced $d-p$ hybridization. Consistent with the experimental results, density functional theory calculations confirm the bulk AFM ordering and a drop in the band gap of the doped samples. We further claim the low-temperature magnetic state of $Y_2Ru_2O_7$ to possess a noncollinear all-out-type spin configuration, which transforms into a randomized glassy phase upon hole doping.

DOI: [10.1103/PhysRevB.109.184423](https://doi.org/10.1103/PhysRevB.109.184423)

I. INTRODUCTION

Since the last few decades, strongly correlated transition metal (TM) oxides have been drawing tremendous research interest as a model platform to realize various exotic quantum phenomena including high-temperature superconductivity [1], heavy fermions [2], colossal magnetoresistance [3–5], and charge density waves [6]. The base material system that hosts these fascinating properties is referred to as a Mott insulator (MI) [7]. In a single-band picture, MIs represent a typical prototype example of correlated systems, in which the stronger on-site Coulomb interaction (U), being larger than the electronic bandwidth (W), causes splitting of the partially filled d band (valence band) into a fully filled lower Hubbard band (LHB) and an empty upper Hubbard band (UHB). In the absence of any other competing interactions, such a splitting of the valence band leads to carrier localization. However, in real materials, the complex interplay of multiple degrees of freedom involving charge, spin, orbital, and lattice [8–11] softens these electronic states. As a result, any external perturbation such as chemical pressure, temperature, strain, or magnetic field triggers an insulator-to-metal transition (also known as Mott transition). Since cation substitution effectively tunes either the bandwidth or causes band filling, metal-insulator transitions (MITs) have been demonstrated in several correlated oxides such as $Y_{1-x}Ca_xTiO_3$ [12]

and $R_{1-x}Sr_xMnO_3$ [13]. However, the electronic interactions and in turn the charge transport characteristics become even more puzzling for systems with heavier TM ions ($4d/5d$ TM ions) because the large spatial extent of the corresponding d orbitals enhances the effective $d-d$ hopping (t), which competes with U . There are also additional competing interactions involving the intra-atomic Hund's coupling (J_H) and spin-orbit coupling (SOC; λ) [14,15]. Furthermore, the intertwining of spin-charge-orbital degrees brings about various unusual noncollinear magnetic structures. The $4d$ -electron-based ruthenates offer an appealing platform to comprehend the connection between MIT and localized magnetism. Based on the structural motifs and corresponding crystal field environments, ruthenates with either Ru^{4+} or Ru^{5+} ions exhibit a large variation in their conducting behavior and effective magnetic moment. While the perovskite ruthenates with Ru^{4+} ions in an octahedral environment are conducting, the pyrochlore ruthenates ($A_2Ru_2O_7$, where A is a rare earth ion or Y) with a similar crystal field are insulating which is primarily attributed to the ratio U/W (where W is one electron bandwidth) [16]. On the other hand, the Ru^{5+} -based ruthenates with half-filled t_{2g} orbitals possess both localized and itinerant character owing to the A site and Ru ($p-d$) hybridization resulting in a bad metal phase, e.g., $Ca_2Ru_2O_7$ [17], and temperature-induced MIT, e.g., $Hg_2Ru_2O_7$ [18]. While the electronic dichotomy and its related MIT have been explained based on the effective U/W , t/J_H , and relative ($p-d$ or $d-d$) hybridization, there is still a lack of a comprehensive understanding of the local magnetism and the effective moment at the Ru site.

In a recent study by Kaneko *et al.* [19], the band-filling controlled MIT has been reported in the electron-doped

*Present address: Institute of Advanced Simulation, Forschungszentrum Jülich, 52425 Jülich, Germany.

†niharika@iitbbs.ac.in

pyrochlore $(\text{Pr}_{1-x}\text{Ca}_x)_2\text{Ru}_2\text{O}_7$. The metallic state is shown to be accompanied with a noncollinear ferromagnetic (FM) state. Furthermore, the observation of a large topological Hall effect implies the emergence of a scalar spin chirality which has been proposed to arise due to the interaction of the Ising Pr $4f$ moments with that of Ru $4d$ spins. However, the FM metallic state with spin chirality was only detected at lower Pr concentrations ($x < 0.5$). Since it is trivial to anticipate that the $4f - 4d$ coupling will be stronger in the case of Pr-rich samples, the proposed mechanism based on these findings appears to be ambiguous.

The most perplexing fact in the metallic, bad metal phases of the pyrochlore is the net/effective magnetic moment (μ_{eff}) associated with the Ru ions, which is found to be screened. For example, the experimentally observed μ_{eff} in the paramagnetic state of $\text{Ca}_2\text{Ru}_2\text{O}_7$ is only $0.36 \mu_B/\text{Ru}$ which is one order less than that expected for the $4d^3$ configuration of the Ru ions [17]. However, such an aspect in the parent and doped samples has largely been ignored. Tuning to the insulating counterpart without $4f$ moments, $\text{Y}_2\text{Ru}_2\text{O}_7$ (YRO) shows a highly frustrated antiferromagnetic (AFM) ground state with an apparent gap in the spin-excitation spectrum as substantiated by the inelastic neutron diffraction experiments [20]. However, the exact Ru spin configuration in YRO and the estimation of this gap in an insulating state have not yet been explored.

Therefore, in this paper, we consider it worthwhile to investigate the prototypical system $(\text{Y}_{1-x}\text{Ca}_x)_2\text{Ru}_2\text{O}_7$ and examine the interplay of $U + J_H$, t , and $d - p$ hybridization in it to understand the enhanced conducting behavior with suppressed net magnetic moment of Ru. Very few studies on $(\text{Y}_{1-x}\text{Ca}_x)_2\text{Ru}_2\text{O}_7$ exist, and most of them have reported on the overall increase in the conductivity and a reduction of T_N . However, a detailed analysis and the correlation between the electronic-transport properties and magnetism is still lacking. Our experimental and density functional theory (DFT) calculations results together point out that the increase in itinerant character of the d electrons induces randomness in magnetism as reflected by the increased frustration parameter and conductivity along reduced T_N . Moreover, the electronic and magnetic structure analysis carried out from DFT revealed the magnetic structure of $\text{Y}_2\text{Ru}_2\text{O}_7$ to be a noncollinear type with an all-out spin configuration giving rise to an AFM order, which gets randomized to a glassy magnetic state by Ca doping.

II. EXPERIMENTAL METHODS

Polycrystalline samples of $(\text{Y}_{1-x}\text{Ca}_x)_2\text{Ru}_2\text{O}_7$ ($0 \leq x \leq 0.6$) were synthesized by the standard solid-state reaction method. Highly pure metal oxides (Y_2O_3 , and RuO_2) and carbonates (CaCO_3) were mixed in stoichiometric ratios, and the mixtures were homogenized by planetary ball milling for 1 h at 300 rpm. These mixed powders were transferred into alumina crucibles and subsequently calcined at 800°C for 12 h in air. The precursor powders were again ground, pressed into pellets, and sintered at 1150°C for 48 h in air. The grinding and sintering cycle was repeated several times until we obtained single-phase samples. The phase purity and structural characterization of the synthesized specimens were performed

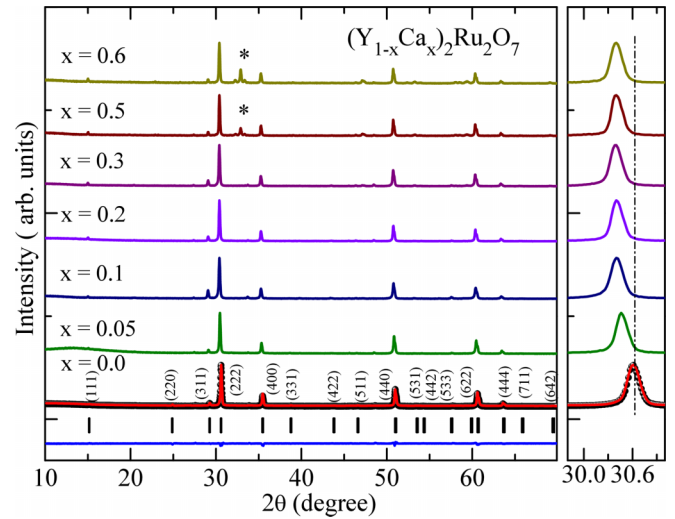


FIG. 1. Room-temperature x-ray diffraction (XRD) pattern along with Rietveld analysis for $(\text{Y}_{1-x}\text{Ca}_x)_2\text{Ru}_2\text{O}_7$ series.

by collecting powder x-ray diffraction (XRD) spectra using a Bruker D8 Advance diffractometer (40 kV, 40 mA) with Ni-filtered $\text{Cu } K\alpha$ radiation with wavelength $\lambda = 1.54184 \text{ \AA}$ at room temperature. The stoichiometry of the samples was determined using an energy dispersive x-ray spectrometer with the help of a field emission scanning electron microscope (FE-SEM; Merlin Compact with GEMINI-I column, Zeiss Pvt. Ltd, Germany). Magnetization measurements were performed in a vibrating sample magnetometer attached to the Quantum Design Physical Property Measurement System. The conventional four-probe technique was used to measure the electrical transport properties.

III. RESULTS AND DISCUSSIONS

A. Structural characterization

Figure 1 shows the room-temperature powder XRD patterns for the $(\text{Y}_{1-x}\text{Ca}_x)_2\text{Ru}_2\text{O}_7$ (YCRO) series of samples with $x = 0 - 0.6$. The diffraction peaks in the XRD spectra of the parent compound, which crystallizes in a face-centered cubic unit cell with $Fd\bar{3}m$ space group symmetry, are consistent with the studies reported earlier [21]. With the substitution of Ca^{+2} for Y^{+3} , there is no significant modification in the crystal structure. However, an expanded view of the XRD pattern around the main diffraction peak at 30.6° [corresponding to the crystal plane (222)] illustrates a gradual shift toward a lower angle (2θ), indicating an expansion of the unit cell with doping. The lattice parameters and other structural features of the doped samples were obtained by the Rietveld refined program using the FULLPROF software package. Analysis of XRD spectra indicates that all the samples with $x \leq 0.3$ are phase pure (without any trace of impurities) and retain the pyrochlore structure. A further increase in the Ca doping concentration resulted in the appearance of a few minor diffraction lines presumably from the unreacted Y_2O_3 phase. It is worthwhile to mention that the fully Ca-substituted member $\text{Ca}_2\text{Ru}_2\text{O}_7$ has been synthesized under high-pressure conditions [17]. Similarly, the Ca-rich members

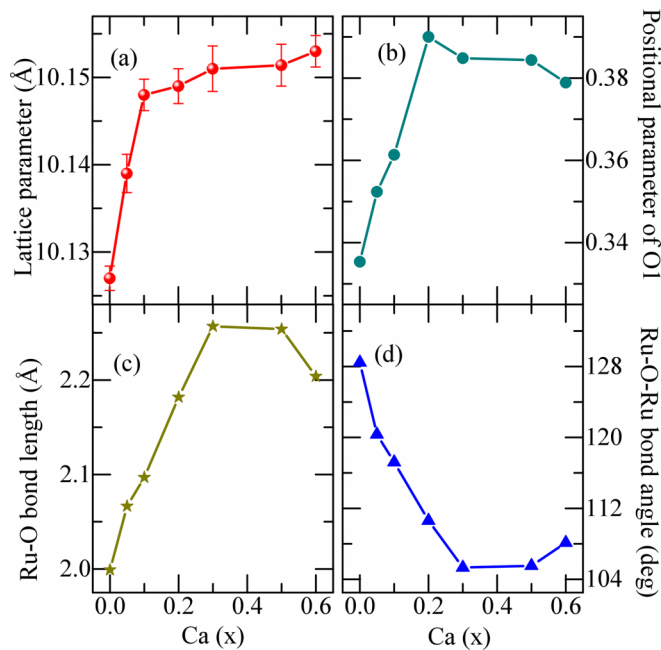


FIG. 2. (a) Lattice parameter a , (b) positional parameter x of O1 atom, (c) Ru-O bond length, and (d) Ru-O-Ru bond angle as a function of Ca substitution for $(Y_{1-x}Ca_x)_2Ru_2O_7$ series.

of the series $(Pr_{1-x}Ca_x)_2Ru_2O_7$ were stabilized only under the high-pressure synthesis method. Further, since Y_2O_3 is nonmagnetic, the magnetic properties of the Ca-rich samples ($x = 0.5$ and 0.6) will not be affected. All the Rietveld fits of XRD profiles are shown in Table SI in the Supplemental Material [22]. The results of $x = 0.4$ are shown in Appendix A in the Supplemental Material [22]. It may be observed that there is an enhancement of the lattice constant parameter with the increase in the Ca^{2+} doping concentration as depicted in Fig. 2(a). The lattice parameter is expected to increase owing to the replacement of a smaller Y^{3+} ion (104 pm) by a larger Ca^{2+} (114 pm) ion. However, a nearly saturated behavior of the lattice parameters was observed for $x > 0.3$, possibly indicating the substitution limitation of YRO in ambient conditions. It should be noted that the variation of the lattice parameter does not follow Vegard's law, which is often maintained when the bonding character is comparable. The variation in Vegard's law in this series is attributed to the distinct bonding character between Y-O and Ca-O. The bonding character between Y and O is covalent, whereas Ca-O is mostly acquired ionic bonding. The partial substitution of Ca in place of Y induces the steric effect and leads to a contraction in bond length. A similar observation of nonlinear lattice expansion has also been reported in Ca-doped $Cd_2Ru_2O_7$ [23]. The FE-SEM micrographs (shown in Fig. S1 in the Supplemental Material [22]) of all the synthesized samples show well-distributed granular submicron-sized particles. Additionally, the energy dispersive x-ray spectroscopy mapping of the YCRO elements clearly indicates the presence of all these elements in the desired stoichiometry.

A schematic view of the cubic pyrochlore structure of YRO is shown in Fig. 3. Each unit cell of this structure has 8 f.u.,

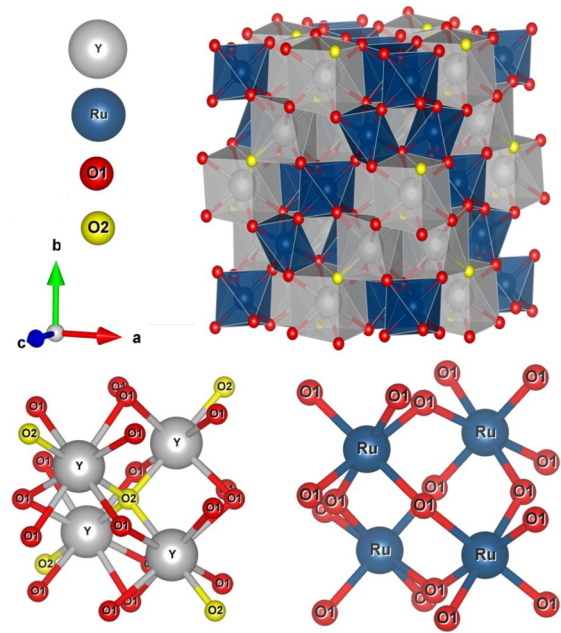


FIG. 3. (a) Unit cell of $Y_2Ru_2O_7$, (b) arrangement of Y tetrahedral and coordinations with O1 and O2 anions, and (c) arrangement of Ru tetrahedral and coordinations with O1 anions.

which is often represented as $Y_2Ru_2(O1)_6(O2)$. In this structure, the Y^{3+} and Ru^{4+} ions occupy the $16d$ ($\frac{1}{2}, \frac{1}{2}, \frac{1}{2}$) and $16c$ (0, 0, 0) sites respectively. For the oxygen anions, O1 occupies the $48f$ ($p, \frac{1}{8}, \frac{1}{8}$) site, while O2 occupies the $8b$ ($\frac{3}{8}, \frac{3}{8}, \frac{3}{8}$) site. Among these four nonequivalent atomic positions, p is the only adjustable parameter, and the coordination polyhedra of the cations change according to the value of this p parameter. Therefore, the O1 p parameter is critical in determining the coordination environment of Y/Ru site ions. When p takes the value 0.315, a perfect octahedron is expected about the $16c$ (Ru) site, while a perfect cube is expected about the $16d$ (Y) site for $p = 0.375$. Otherwise, an axially compressed or extended scalenohedron is formed about the Y/Ru site when $x < 0.375$ and $x > 0.375$, respectively. From the analysis of our XRD data, we obtained a p value of 0.335, suggesting compressed and distorted octahedra about the Ru site (RuO_6).

The distinct crystallographic features of this pyrochlore structure include the interplay of two interpenetrating but independent networks of Ru-centered (B_2O_16) octahedra and A_2O_2 zigzag chains. The O2 anions are tetrahedrally coordinated with Y^{3+} ions, forming the O_2Y_4 moiety, while the O1 anions are also tetrahedrally coordinated but with both Y^{3+} and Ru^{4+} ions forming the $O_1Y_2Ru_2$ moiety. Interestingly, the structural organization of both $16c$ (Ru^{4+}) and $16d$ (Y^{3+}) sites constitutes a three-dimensional (3D) array of corner-sharing tetrahedra. The tetrahedral coordination of the magnetic Ru^{4+} ions develops into a highly frustrated geometric lattice. Moreover, due to the presence of Y^{3+} ions at the interstitial positions of B_2O_16 octahedra, it is essentially distorted reducing the Ru^{4+} -O1- Ru^{4+} bond angle much lower than 180° ($\sim 130^\circ$). It is also expected that the lattice geometries would further be modified by doping at the A site. Since the magnetic exchange interaction and the conducting proper-

ties of the pyrochlores are influenced by the Ru^{4+} -O1- Ru^{4+} bond/angle and Ru^{4+} coordination environment, we analyzed the doping-dependent modification of the positional parameter of O1 (value of the x parameter) and Ru^{4+} -O1- Ru^{4+} bond length/angle, shown in Figs. 2(b)–2(d). One may notice a systematic increase of the x parameter and bond length and a decrease of the bond angle with the doping concentration x . However, beyond the doping level of $x = 0.3$, these parameters essentially saturate possibly due to the substitution limitations. It is interesting to note that the decrease in bond angle, i.e., being further $<130^\circ$, suggests a possible weakening of the strength of the Ru-Ru AFM interaction. The A-O1 and Ru-O1 bond length depends on both positional parameters and lattice constants, while the shorter A-O2 depends only on the lattice constant. An increased value of x implies the distortion of the RuO_6 octahedra to be higher than that of the parent sample, which may further enhance the crystal field and the frustration.

B. Magnetic properties

The temperature dependence of the magnetic susceptibilities $\chi (= M/H)$, measured in an applied field of 5000 Oe under zero-field-cooled (ZFC) and field-cooled (FC) protocols of all the specimens, are shown in Fig. 4. For the parent YRO compound, one may notice an apparent divergence of ZFC and FC susceptibilities <80 K (T_{irr}) [as shown in the inset of Fig. 4(a)]. At this temperature, a cusp is observed in the χ_{ZFC} curve, while χ_{FC} exhibits sudden enhancement, implying the onset of magnetic ordering. This result is consistent with the neutron diffraction and μSR studies and agrees well with the previous reports [24]. We also note that T_{irr} and T_N coincide for the pristine sample. Extending our study to the Ca-doped samples, we observed that the divergence of χ_{ZFC} and χ_{FC} curves and the cusp in χ_{ZFC} appear at two separate temperatures. While T_{irr} decreases marginally for low Ca doping concentration and then sharply for higher Ca doping concentration, the cusp temperature (T_N) falls gradually and essentially linearly with x [see Figs. 5(a) and 5(b)]. For some of the intermediate compositions (e.g., $x = 0.3$), χ_{ZFC} exhibits two cusp features as if there is a competition/coexistence of two magnetically distinct phases. Due to the substitution of Ca at the Y site, which is a bit of a random substitution (instead of statistical distribution), a fraction of Ru ions may get disconnected from the original all-out arrangements. These Ru moments, which do not take part in the all-out AFM ordering like the parent compound, get frozen at a lower temperature, resulting in a spin-glass phase. With a further increase in doping concentration (e.g., for $x = 0.6$), the ZFC and FC susceptibility behavior was found to resemble that of a spin glass. The ZFC curve displays a sharp fall at low temperatures trailing a peak of ~ 14 K, whereas the FC curve shows a monotonous increase without any signature of saturation as if the spin states and the associated magnetic frustration get disrupted by the Ca doping.

To understand the doping-induced modification of the Ru spin states, we analyzed the high-temperature paramagnetic susceptibility of all the samples. The $\chi^{-1}(T)$ shows linear behavior (see Fig. S2 in the Supplemental Material [22]) in the high-temperature range ($T > 150$ K), and therefore, the

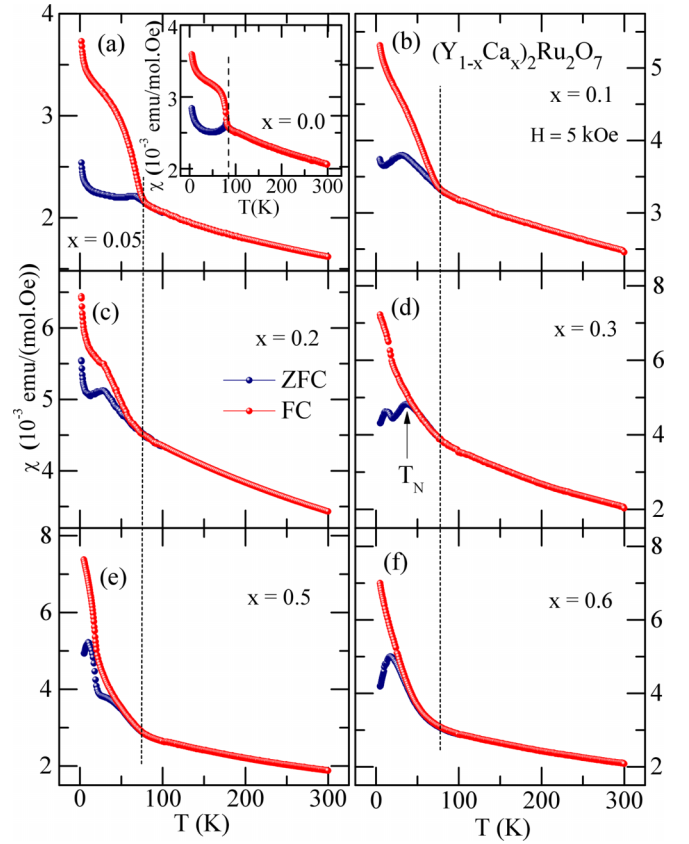


FIG. 4. (a)–(f) Magnetic susceptibility as a function of temperature in both zero-field-cooled (ZFC) and field-cooled (FC) conditions with an externally applied field of 5 kOe for $(\text{Y}_{1-x}\text{Ca}_x)_2\text{Ru}_2\text{O}_7$ series ($x = 0.05, 0.1, 0.2, 0.3, 0.5, \text{ and } 0.6$). The inset of (a) represents the ZFC and FC data of the parent sample ($x = 0.0$). The dashed line acts as the reference (a guide to the eye) against which one can observe the variation of the irreversible temperature in doped samples relative to that of the pristine.

data were fitted with the Curie-Weiss (CW) law:

$$\chi = \frac{C}{T - \theta_{\text{CW}}}, \quad (1)$$

where C and θ_{CW} are the Curie constant and CW temperature, respectively. The values of θ_{CW} and μ_{eff} (deduced from the Curie constant) for the parent sample agree with the previously reported results [25]. Like the parent compound, θ_{CW} is found to be negative for all the doped samples, suggesting the dominance of AFM correlation. However, the magnitude of θ_{CW} gradually decreases with the doping concentration x as may be seen in Fig. 5(b), which suggests a weakening of the AFM coupling. We further tried to estimate the frustration parameter [$f = \theta_{\text{CW}}/T_N$] as a function of doping. As depicted in Fig. 5(c), the frustration parameter increases with x , implying that the primary magnetic structure of the pristine might have been disrupted by this doping and leads toward a more frustrating system. In Fig. 5(d), we have shown the variation of the calculated effective paramagnetic moment μ_{eff} [26] for all the doped samples. The obtained value of $\mu_{\text{eff}} (= 3.2 \mu_B/\text{Ru})$ for the parent YRO compound is marginally higher than the theoretically expected spin-only

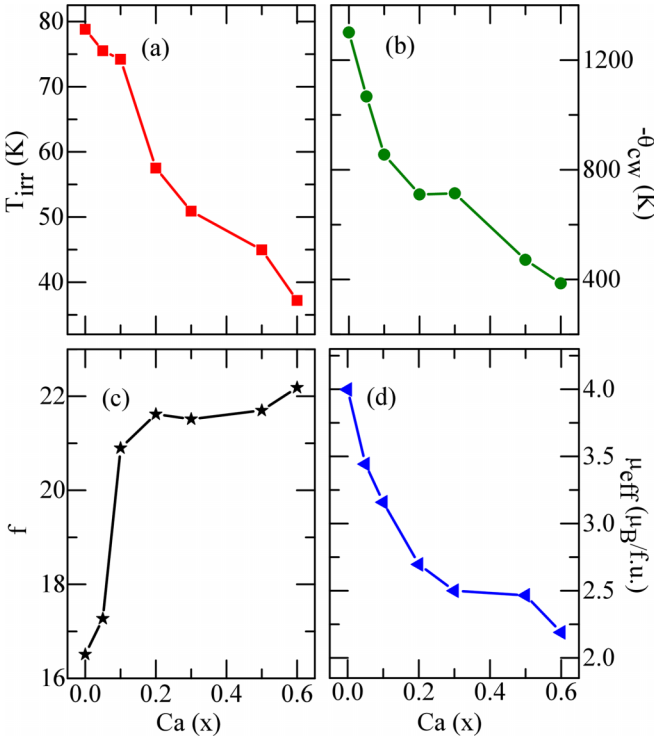


FIG. 5. Variation of (a) the irreversible temperature (T_{irr}), (b) Curie-Weiss temperature ($-\theta_{\text{CW}}$), (c) frustration parameter ($f - |\theta_{\text{CW}}|/T_N$), and (d) effective magnetic moment (μ_{eff}) of $(Y_{1-x}\text{Ca}_x)_2\text{Ru}_2\text{O}_7$ as a function of Ca doping concentration (x).

value of $(g\sqrt{S(S+1)}\mu_B) = 2.82\mu_B/\text{Ru}$. However, the results obtained through neutron and μSR studies yield $1.36\mu_B/\text{Ru}$ in the long-range ordered state. This reduction of the Ruthenium moment in the ordered state has been described in detail by Kmieć *et al.* [24], considering all the aspects including axial crystal-field splitting and SOC, which was finally attributed to the additional splitting of energy levels due to SOC. This value also suggests that Ru^{4+} ($4d^4$) is in a low-spin state, where all the d electrons occupy the $4d - t_{2g}$ orbital; Ru^{4+} ($4d^4$; $t_{2g}^3 \uparrow t_{2g}^1 \downarrow e_g^0 \uparrow e_g^0 \downarrow$) with $S = 1$. As evident from Fig. 5(d), μ_{eff} decreases monotonously with increasing Ca concentration in the YRO lattice. The previous x-ray photoelectron spectroscopy studies on divalent (Ca^{2+} , Zn^{2+} , Ba^{2+}) ion-doped YRO samples have claimed the presence of mixed-valence states of Ru (Ru^{+4} and Ru^{+5}) [27–29]. Therefore, it is trivial to assume that our Ca-doped samples contain mixed valence states of Ru. However, it could be expected that, due to the presence of Ru^{+5} (considering the localized state) in the system, the moment should increase as it is present in the $S = \frac{3}{2}$ state ($4d^3$; $t_{2g}^3 \uparrow t_{2g}^0 \downarrow e_g^0 \uparrow e_g^0 \downarrow$). At this juncture, it is worthwhile to recall that the experimentally observed μ_{eff} value of $\text{Ca}_2\text{Ru}_2\text{O}_7$ [17], in which all the Ru ions are in the $5+$ state, is $\sim \frac{1}{10}$ times smaller than that expected for a free Ru^{5+} . One of the possible causes of the reduced moment could be due to the additional splitting of t_{2g} levels owing to the impact of strong L-S coupling. Nonetheless, the reported theoretical band structure calculations have ruled out such a possibility. Alternatively, itinerancy of the d orbitals or its hybridization with the Ca/O p orbital states may be affecting the overall

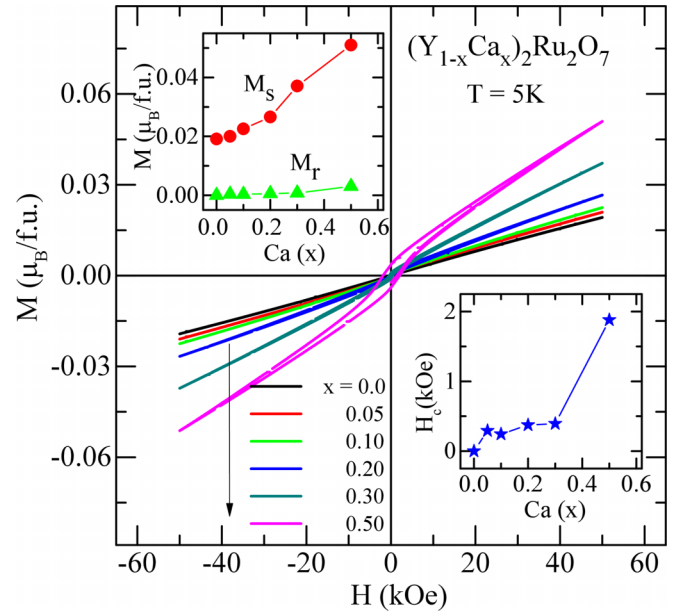


FIG. 6. Magnetic isotherms measured at the temperature 5 K. The upper inset shows the saturation magnetization (M_S) and remanent magnetization (M_R). The lower inset represents the coercive field (H_C) as a function of Ca doping concentration (x).

effective moment. Such a deviation in the effective moment has also been reported for another itinerant character-based ruthenium pyrochlore $\text{Hg}_2\text{Ru}_2\text{O}_7$, which shows strong $p - d$ hybridization [30,31].

To get more insight into the magnetic characteristics of the doped samples, we measured magnetization as a function of magnetic field (H) for all the samples at selected temperatures. Figure 6 presents the $M(H)$ behavior of the doped samples at 5 K with respect to that of the pristine. As seen in the figure, there is a systematic increase in the net magnetization with the doping level. Additionally, a noticeable hysteresis loop is observed for the sample with $x = 0.5$. Though $M-H$ curves of the doped compounds do not show saturations up to 5 T magnetic field, there is an inducement of a FM/ferrimagnetic component possibly due to a spin canting caused by the Ca doping in the YRO lattice. In the inset of Fig. 6, we have shown the variation of the maximum M value (M_S) for an applied field of 5 T and the remanent magnetization (M_R) as a function of the doping concentration. The increasing trends of both M_R and M_S indicate the enhancement of magnetocrystalline anisotropy along with a small FM correlation.

To understand the nature of the magnetic state in further detail, we have analyzed magnetization data from the Arrott plots (M^2 vs H/M ; see Fig. S3 in the Supplemental Material [22]). The detailed significance of the Arrott plot is discussed elsewhere [24,32]. One may notice from these plots that the intercept of a straight-line fitting to the M^2 values turns out to be negative for all the compounds, indicating that none of the low-temperature magnetic states in $\text{Y}_2\text{Ru}_2\text{O}_7$ are FM in nature. Additionally, it signifies that adding Ca in $\text{Y}_2\text{Ru}_2\text{O}_7$ does not promote FM in this material. The previous neutron and μSR measurements on the parent compound specify complex AFM ordering with strong magnetic frustration [24]. As illustrated, this ordering gets disrupted with Ca doping. Moreover,

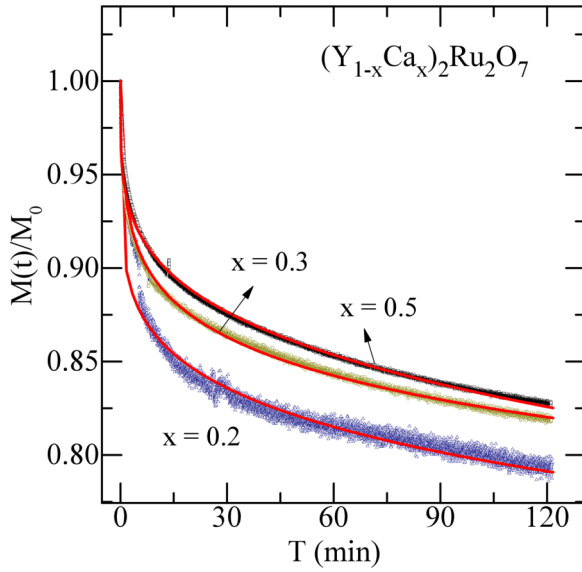


FIG. 7. The normalized isothermal remanent magnetization as a function of time at 5 K for $(Y_{1-x}Ca_x)_2Ru_2O_7$ with $x = 0.2, 0.3,$ and 0.5 . The solid line through the data points represents the fit with the stretched exponential model as described in the text.

we have also shown an increase in the frustration parameter with an enhancement of the coercivity. This suggests a possibility of the development of a glassy magnetic phase.

To understand the nonequilibrium characteristics related to the presence of the glassy magnetic state in the doped specimens, we have recorded the time evolution of magnetic moments for Ca-substituted samples via isothermal remanent magnetization (M_{IRM}) measurements. Since the glassy magnetic systems have various metamagnetic states, the moment in this case evolves with time even while the magnetic field and temperature remain constant. We measured the relaxation of the moment following a protocol where the sample is cooled from room temperature to the desired temperature in zero field. After stabilizing the temperature, a magnetic field of 5000 Oe is applied for 600 s. Subsequently, the M_{IRM} data were measured as a function of time (t) in zero field, which are presented in Fig. 7. At low temperature (say, 5 K), the normalized M_{IRM} of the compounds with $x = 0.20, 0.30,$ and 0.50 exhibit slow time decay, as expected for spin-glass systems [33]. It is worthwhile to mention that the M_{IRM} data for compounds with $x = 0.00, 0.10$ quickly set to a negligible value and did not exhibit slow decay of moment with time (please see Fig. S4 in the Supplemental Material [22]). This signifies that the glassy magnetic character has been developed in the doped specimens above a certain level of Ca doping.

To understand the mechanism that drives the system back to the equilibrium state, we tried to fit the relaxation behavior to the functional forms describing different spin dynamics [34–41]. The parent compound is observed to exhibit long-range AFM ordering. However, the glassy state in the doped sample would arise due to the coexistence and competition of AFM and FM interactions. The glassy behavior is initially fitted with power law function as given in Eq. (2). Monte Carlo simulations of 3D Ising spin glass has validated the

applicability of this model to spin-glass systems as well [42]:

$$M(t) = M_0 t^{(-\gamma)}, \quad (2)$$

where M_0 and γ are the fitting parameters. The exponent γ is the function of temperature and applied field. However, our observed data deviate largely from this model, as demonstrated in Fig. S5 in the Supplemental Material [22]. The second type of functional form used for modeling the relaxation curve is the logarithmic dependence on time [38–41], which describes systems having energy barriers uniformly distributed from zero to a certain maximum value, as shown in the following:

$$M(t) = M_0 - C \ln(t). \quad (3)$$

Here, M_0 is the initial magnetization at time zero, and C represents the magnetic viscosity which is a constant for a specific temperature, field, and material. The Néel theory of superparamagnetism has been used to interpret this logarithmic dependence of remanent magnetization. Numerous spin-glass systems have shown agreement with this model. As depicted in Fig. S5 in the Supplemental Material [22], this model also fails to explain the time decay of magnetization for the doped YRO system, which may be due to the presence of a distribution of relaxation times. In this scenario, the stretched exponential decay function [43–48] is the most frequently used function for simulating the remnant magnetization data, which is expressed as follows:

$$M(t) = M_0 \exp(-t/\tau)^n, \quad (4)$$

where n and M_0 are the fitting parameters linked to the glassy component of magnetization. Here, M_0 is the initial magnetization at time zero, whereas τ represents the characteristic relaxation time. The energy barriers involved in the relaxing process affect the value of n . While $n = 1$ reveals that the system relaxes with a single time constant, $n = 0$ implies the absence of any relaxation. For spin glasses, n takes a value between 0 and 1. Our observed data show very good agreement with the stretched exponential function over the whole time scale, as depicted in Fig. 7. For comparison, we have also presented the power law and logarithmic functions (please see Fig. S5 in the Supplemental Material [22]), which do not mimic the initial part of the relaxation behavior. The parameters M_0 and τ obtained from the best are summarized in Table SII in the Supplemental Material [22]. It is apparent from the fitting data that Ca doping tries to shorten the relaxing time, which reduces from $\tau \sim 2.46 \times 10^8$ (for $x = 0.2$) to $\tau \sim 1.65 \times 10^7$ (for $x = 0.5$). On the other hand, the stretching exponential (n) increases as we increase the Ca concentration in the lattice. The obtained relaxation time τ and n (~ 0.17817) for $(Y_{1-x}Ca_x)_2Ru_2O_7$ ($x = 0.5$) are in good agreement with the corresponding values for classical spin-glass systems such as Ag : Mn [49]. However, in comparison with molybdenum-based pyrochlore systems ($R_2Mo_2O_7$: $R = Y, Sm, Ho$), the experimental relaxation rate ($\tau \sim 10^5 - 10^6$ s) carries two orders of magnitude lower [50]. When comparing with the Cr- and Ru-doped $Y_2Ir_2O_7$ ($\tau \sim 10^8 - 10^9$), it falls within the range of our experimental findings [51,52]. For such a reduction in τ and simultaneously enhanced value of n through the series, though indicative of higher frustration and relaxation behavior, the small n value ($< \frac{1}{3}$) suggests the

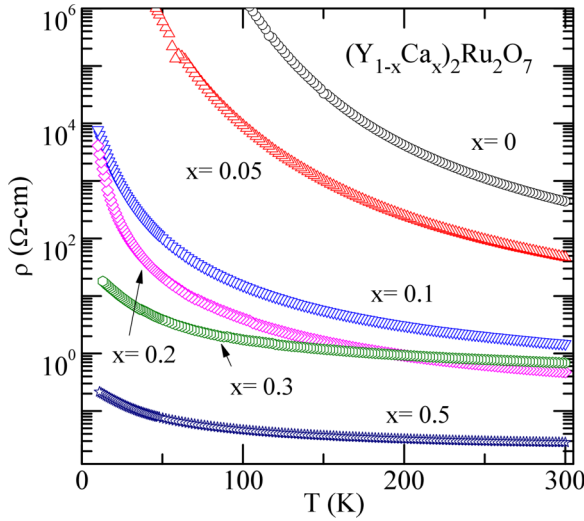


FIG. 8. Temperature dependence of resistivity for $(Y_{1-x}Ca_x)_2Ru_2O_7$ in semilog plot.

presence of a disruptive or clustered AFM state along with the glassy phaselike phase separation.

C. Electrical resistivity

To investigate the effect of Ca substitution on the charge transport characteristics of YRO, electrical resistivity (ρ) measurements were carried out as a function of temperature, which is demonstrated in Fig. 8. The parent sample is known to exhibit insulating behavior in the entire temperature range <300 K [29]. As shown in the plot in Fig. 8, the low-temperature resistivity at ~ 100 K increases by three orders of magnitude in comparison with that at room temperature. With Ca doping, a systematic decrease of resistivity was observed at all temperature ranges. Moreover, this resulted in a weak temperature dependence of $\rho(T)$ for samples with higher Ca doping up to $x = 0.5$. On the other hand, a further enhancement of the doping ($x = 0.6$) causes a higher value of $\rho(T)$ (see Fig. S6 in the Supplemental Material [22]), presumably due to the enhancement of impurity-induced scatterers, as this sample was detected with the presence of unreacted Y_2O_3 as a secondary phase. Therefore, the rest of our discussion on transport properties is limited to the doping level up to $x = 0.5$.

The significant enhancement of the conductivity with Ca doping can be understood on the framework of hole doping. An established mechanism involved with Ca doping in YRO is to convert a part of Ru^{4+} ions into Ru^{5+} yielding a mixed valent state of Ru. Previous reports on the x-ray photoelectron spectroscopy studies of $(Y_{1-x}Ca_x)_2Ru_2O_7$ have also confirmed the presence of Ru^{5+} ions [53]. Ru^{4+} has a well-defined spin state ($S = 1$) with all localized electrons, while there is not enough clarity on the electronic configuration of Ru^{5+} and its effective J value. Though the SOC strength of Ru^{5+} ions is neglected in most of the calculations, the estimated spin state of Ru^{5+} ($S = \frac{3}{2}$) never agrees with the effective moment value obtained from the CW behavior. Furthermore, if we consider the localized $S = \frac{3}{2}$ state of

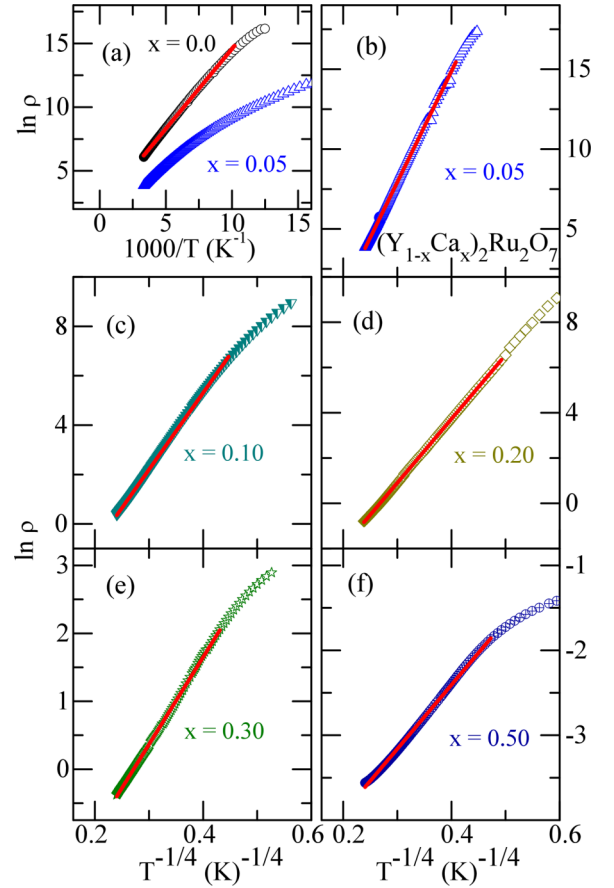


FIG. 9. (a) Resistivity data of $x = 0.0$ and 0.5 samples as a function of inverse temperature. The solid red line in the undoped sample is fitted by an Arrhenius-type law. (b)–(f) The logarithm of $\rho(t)$ with $T^{-1/4}$ for $x = 0.05, 0.10, 0.20, 0.30,$ and 0.50 . The solid red line is the least square fit to the three-dimensional Mott variable-range-hopping model.

Ru^{5+} , the metal-like conductivity and the magnetic state of $Ca_2Ru_2O_7$ cannot be explained.

To understand the charge transport mechanism in the doped samples, we have fitted the models proposed for MIs such as Arrhenius behavior (thermally activated model), and Mott's variable range model as shown below [Eqs. (5) and (6), respectively]:

$$\rho(T) = \rho_0 \exp\left(\frac{E_a}{k_B T}\right), \quad (5)$$

where E_a represents the activation energy, and k_B is the Boltzmann constant, and

$$\rho(T) = \rho_0 \exp(T_0/T)^{1/4}, \quad (6)$$

where T_0 is the characteristic temperature, related to the density of localized states at the Fermi level $N(E_f)$ and the localization length of the carriers ξ ($= \alpha^{-1}$), as follows:

$$T_0 = \frac{\lambda \alpha^3}{k_B N(E_f)}, \quad (7)$$

where λ is a dimensionless constant (≈ 18) related to the hopping probability, and α is the spatial extension of the wave

TABLE I. Variation of Mott's characteristic temperature T_0 , Mott's hopping range R , and energy parameter for temperature range 50–250 K.

Sample	T_0 (K)	R (m)		W (meV)	
		300 K	50 K	300 K	50 K
$(Y_{1-x}Ca_x)_2Ru_2O_7$					
0.05	2.31×10^7	6.32×10^{-9}	9.90×10^{-9}	107.0	28.1
0.10	9.21×10^5	2.83×10^{-9}	4.43×10^{-9}	48.0	12.5
0.20	6.32×10^5	2.57×10^{-9}	4.03×10^{-9}	43.8	11.43
0.30	2.68×10^4	1.17×10^{-9}	1.83×10^{-9}	19.87	5.18
0.50	1.71×10^4	1.04×10^{-9}	1.63×10^{-9}	17.7	4.61

function $e^{(-\alpha R)}$ associated with the localized states. Here, T_0 also represents the degree of disorder.

As depicted in Fig. 9(a), the $\rho(T)$ data of the pristine can be nicely fitted by the Arrhenius-type behavior. A linear fit of $\ln \rho$ with $1000/T$ yields activation energy related to the hopping conduction of the localized carriers as $E_a \approx 0.1$ eV. This is consistent with the Mott-Hubbard insulating behavior reported previously for $Y_2Ru_2O_7$ [54]. In the same graph, we also show the $\rho(T)$ behavior of the compound with $x = 0.05$, which is apparently nonlinear in the entire temperature range, suggesting that the conduction behavior is not Arrhenius type for the doped samples. Nonetheless, a good agreement of the $\rho(T)$ data with the Mott's variable-range hopping (VRH) type conduction behavior was obtained for all the doped samples, as evident in Figs. 9(b)–9(f). According to Mott's formalism, we have considered the localization length ξ as equal to the lattice parameter. Based on this model, the hopping distance R_h and hopping energy W_h can be derived using the following expression [55–57];

$$R_h = \frac{3}{8} \xi \left(\frac{T_0}{T} \right)^{1/4} \quad \text{and} \quad W_h = \frac{1}{4} K_B T^{3/4} T_0^{1/4}. \quad (8)$$

The resistivity data fit well with Mott's 3D-VRH model, suggesting that the transport is governed by the disorder-induced localization of charge carriers. The fitted T_0 value is listed in Table I. We have estimated the values of R_h and W_h at 300 and 50 K by using Mott characteristic temperature. The results are also summarized in Table I. A careful analysis of the data in Table I indicates that the value of T_0 decreases with increasing the Ca concentration. As T_0 is inversely proportional to the localization length (ξ) and the density of states (DOS) [$N(E_f)$], there is an apparent increase in these parameters leading to higher conductivity. Moreover,

it may also be noticed that R_h increases, while the value of W_h decreases with decreasing temperature. Therefore, one can infer that the electrons experience less scattering at higher temperatures, leading to reduced resistivity, whereas disorder-induced scattering is more at low temperatures, leading to higher resistivity. Furthermore, by enhancing the substitution limit of Ca ions at Y sites, the hopping distance and hopping energy decrease at 300 as well as 50 K. These variations of R_h and W_h signify the system to approach MIT in this series. Furthermore, we find the ratio of $\frac{R_h}{\xi}$ derived from the fitting parameters as >1 in the whole temperature region satisfying the criterion for Mott's VRH.

IV. ELECTRONIC AND MAGNETIC STRUCTURE FROM DFT CALCULATIONS

DFT is the most realistic theory available to examine the electronic and magnetic structure of solids and to substantiate and complement the experimental observations. Therefore, we have carried out DFT calculations to study the electronic and magnetic structure of $(Y_{1-x}Ca_x)_2Ru_2O_7$. Here, we have only considered the cases of $x = 0$ and 0.50, as these represent the two end members of the experimental study. To identify the magnetic ground state, the calculations were carried out on four symmetry-allowed noncollinear magnetic configurations, namely, all-out, all-in-all-out, 3-in-1-out, and 2-in-2-out (see Fig. 10). For the bulk YRO, we have considered experimentally obtained crystal structure, whereas for the doped case, the atomic positions and cell volume were relaxed while keeping the cubic symmetry intact.

The DFT calculations were performed using the projector augmented-wave (PAW) [58] method as implemented in VASP [59]. The generalized gradient approximation was chosen for the exchange-correlation function. The effect of strong corre-

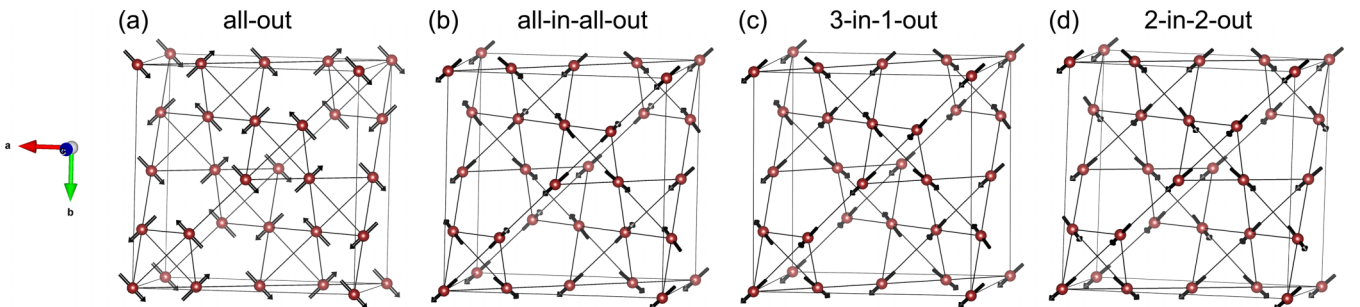


FIG. 10. The depiction of four considered symmetry-allowed magnetic arrangements, namely, all-out, all-in-all-out, 3-in-1-out, and 2-in-2-out, respectively. These antiferromagnetic spin arrangements are designed in such a way that the spins on the Ru atoms either point inward or outward to the Ru tetrahedra.

TABLE II. The relative energy differences E_{rel} in meV/f.u. for the most stable magnetic configuration (all-out), corresponding bulk band gap, and local spin magnetic moment at Ru sites as a function of U_{eff} .

U_{eff} (eV)	All-out	All-in-all-out	3-in-1-out	2-in-2-out	Band gap (eV)	Spin moment (μ_B)
2	0	11	11	41.25	0.17	1.48
3	0	12.41	26.50	35.46	0.91	1.58
4	0	13.34	29.50	31.06	1.42	1.66

lation was incorporated via the effective interaction parameter $U_{\text{eff}} = U - J$ through the rotationally invariant Dudarev's approach [60]. The Brillouin zone integration was carried out using $8 \times 8 \times 8$ and $10 \times 10 \times 10$ k meshes to achieve self-consistency and to obtain the DOSs, respectively. The kinetic energy cutoff for the plane-wave basis set was chosen to be 400 eV. The PAW basis functions include $2s$ and $2p$ orbitals for O; $4s$, $4p$, $5s$, and $4d$ orbitals for Y; $4s$ orbital for Ca; and $4d$ and $5s$ orbitals for Ru.

Though the pyrochlore iridates are extensively studied experimentally and theoretically, to date, the theoretical analysis on pyrochlore ruthenates is missing in the literature. Therefore, it is prudent to first analyze the electronic and magnetic structure of the parent YRO. To do so, we have designed various magnetic configurations, which are shown in Fig. 10. In these configurations various noncollinear AFM arrangements have been considered, such as all-out (all spins pointing outward to the tetrahedra formed by Ru atoms), all-in-all-out (all spins pointing inward in one tetrahedron and outward in adjacent tetrahedra), 2-in-2-out (two spins pointing inward/outward to the tetrahedra), and 3-in-1-out (three spins pointing inward and one outward to the tetrahedra). Table II lists the relative energy differences, band gap, and local spin moment at the Ru site as a function of on-site correlation strength U_{eff} . As inferred from Table II, the all-out magnetic configuration forms the ground state of YRO and is robust against U_{eff} . The all-out magnetic ground state obtained from the DFT + U + SOC calculations agrees with the recent neutron diffraction measurements [24]. The experimental band gap of 1.5 eV for the pristine compound [28,61,62] is realized for $U_{\text{eff}} = 4$ eV. The origin of the band gap formation can be explained by examining the atom-resolved DOS as a function of U_{eff} for the ground state all-out magnetic configuration, which is shown in Figs. 11(a)–11(c). Due to the RuO_6 octahedral crystal field, the fivefold degenerate d states split into a threefold degenerate and low-energy-lying t_{2g} and twofold degenerate and higher-energy-lying e_g states. As evident from the DOS, while the e_g states are unoccupied and lie far above the Fermi level in the conduction band (in the range of 3–5 eV with regard to E_F), the t_{2g} states split into LHB and UHB with a gap in between. The local magnetic moment at the Ru site is calculated to be 1.66 μ_B , which is close to the $S = 1$ state, which agrees with our experimental observation. This further implies the electronic configuration for each Ru to be $4d^4$; $t_{2g}^3 \uparrow t_{2g}^1 \downarrow e_g^0$. Moreover, the Y d states are unoccupied due to the $3+$ charge state; they have a $4d^0 5s^0$ valence configuration. With increasing U_{eff} , the separation between LHB and UHB increases, and hence, the gap increases.

Having understood the ground-state electronic and magnetic structure of the parent YRO, now we analyze the effect

of Ca doping on the electronic and magnetic properties. For this purpose, we have chosen the 50% doping case and designed five different doping configurations (see Fig. 12). These configurations were designed by altering the Ca-Ca and Y-Y bond lengths in this layered structure. Upon structure relaxation, we found the minimum energy configuration [see Fig. 12(a)] to be one wherein the chain configuration in all the layers is of the form Ca-Ca-Y-Y, i.e., the doped Ca atoms are close to each other. Taking this minimal energy-doped configuration, we examine the energetics of different magnetic structures, and the obtained relative energy differences are listed in Table II for $U_{\text{eff}} = 4$ eV. As inferred through Table III, the 3-in-1-out and 2-in-1-out states remain highly

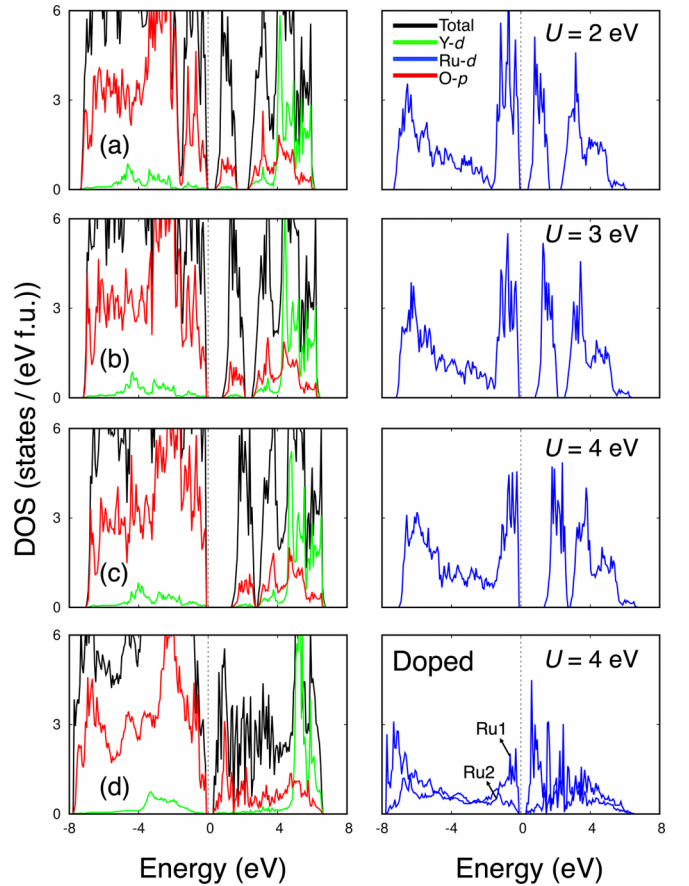


FIG. 11. (a)–(c) The atom and orbital resolved density of states (DOS) of the most stable all-out magnetic configuration as a function of U_{eff} . The band gap increases from 0.17 eV at $U_{\text{eff}} = 2$ eV to 1.44 eV at $U_{\text{eff}} = 4$ eV due to the increasing split in the lower Hubbard band (LHB) and upper Hubbard band (UHB) with increasing on-site correlation strength.

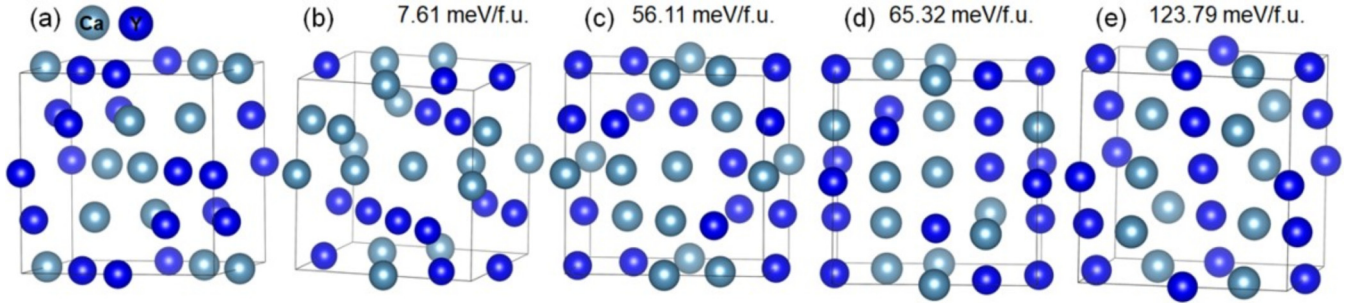


FIG. 12. The various doping arrangements considered for $(Y_{1-x}Ca_x)_2Ru_2O_7$, $x = 0.5$, and their relative energy differences concerning the most stable doping arrangement. In this minimal energy-doped configuration, the Ca atoms are close to each other due to Ca-Ca-Y-Y chain formation. The Ru and O atoms are not shown to bring more clarity.

unstable, as in the case of bulk; however, the all-out and all-in-all-out states are energetically very close to each other. The competition between these two states is suggestive of spin-glass behavior, as the energy difference ($\sim 5K$) is comparable. This is in fact smaller than the energy scale of the spin-glass transition temperature $\sim 14K$ as observed experimentally. A similar observation and inference have been made by Shinaoka *et al.* [63] while pursuing the spin-glass behavior of pyrochlore $Y_2Mo_2O_7$ [63]. This spin-glass behavior is consistent with the experimentally observed spin-glass transition with Ca doping. For the all-out state, the DOS is shown in Fig. 11(d). The band gap reduces to 0.43 eV ($\sim 69\%$ reduction from bulk band gap). The reduction in band gap with Ca doping is indicative of decreasing resistivity in this system which is also observed from the resistivity measurements for the doped sample. The doping of Ca makes the Ru atoms geometrically inequivalent, leading to two inequivalent Ru atoms per formula unit, which we define as Ru1 and Ru2. While the former is tentatively in 4+ charge state with d^4 electronic configuration (as in the pristine system), the latter is tentatively in 5+ charge state with d^3 electronic configuration. A crystal structure identifying Ru1 and Ru2 is provided in the Fig. S7 in the Supplemental Material [22]. The formation of these mixed valence states with doping can be understood by analyzing the DOS. The Ca doping further splits the occupied t_{2g} DOS. A part of the t_{2g} subband is now unoccupied. This unoccupied subband lies below the bulk LHB to reduce the band gap, which implies the distribution of d^4 and d^3 states. The corresponding magnetic moments for these two states are $Ru1 = 1.63 \mu_B$ and $Ru2 = 2.10 \mu_B$, respectively. If we compare the DOS of the pristine [Fig. 11(c)] and doped [Fig. 11(d)] systems, we observe that, in the case of the latter, there is an increase in the width of Ru d dominated bands and an

increase in the overlap of O p DOS with that of the Ru d DOS. Taken together, these features imply the reduction in the localization of the Ru d states through $p-d$ hybridization, and consequently, the doped system exhibits the experimentally observed enhanced conductivity.

V. SUMMARY AND CONCLUSION

Summing up the experimental findings of this paper, we observe Ca doping in YRO leads to (1) a gradual decrease in the Ru-O1-Ru bond angle, (2) an increase in the frustration parameter, (3) reduction of the Néel order temperature and simultaneous development of glassy magnetic phase, and (4) a significant enhancement of the conducting behavior even though the temperature coefficient of resistivity is negative for all the doped samples. There is a clear indication of the itinerant character of Ru^{5+} which replaced the localized Ru^{4+} ions by Ca doping. From our total energy calculations for a variety of magnetic configurations, we see comparable energy for the all-out and all-in-all-out configurations, and it leads to the formation of the glassy state. Getting insight from electronic structure calculations, it may be seen that the DOS of YRO is composed of Ru t_{2g} and O p orbitals near the Fermi level, while there is negligible hybridization between Y and Ru $d/O p$ bands. With Ca doping, the DOS reflects increased bandwidth of the Ru d orbital presumably due to enhanced Ru $d/O p$ hybridization. The screening of the magnetic moment can seemingly be attributed to this increased covalence. It may also be recalled that, in the metallic pyrochlore $Bi_2Ru_2O_7$, the Bi p states are situated near the Fermi energy level and mixed with antibonding states of Ru t_{2g} and O1 p orbitals, whereas the s bands are situated far below the Fermi energy level. Due to this itinerancy, $Bi_2Ru_2O_7$ exhibits a Pauli paramagnetic state with a complete screening of the localized Ru moments. Next, turning to the role of the f electron in inducing the topological FM state in the electron-doped regime of $(Pr_{1-x}Ca_x)_2Ru_2O_7$, this aspect remained unresolved, as the sample synthesis of the electron-doped regime at ambient condition was not conceivable. However, it is worth noting that, in the hole-doped regime of $(Pr_{1-x}Ca_x)_2Ru_2O_7$, the samples exhibiting metallic conductivity are associated with a paramagnetic state. Additionally, μ -spin rotation experiments also revealed that the randomness in magnetism increases with increasing the itinerancy of d electrons [64]. Therefore, the suppression of the effective magnetic moment and develop-

TABLE III. The relative energy differences E_{rel} in meV/f.u. for the most stable magnetic configuration (all-out) for $(Y_{1-x}Ca_x)_2Ru_2O_7$, $x = 0.5$.

Configurations	E_{rel} (meV/f.u.)
All-out	0
All-in-all-out	0.38
3-in-1-out	31.70
2-in-2-out	24

ment of a glassy magnetic phase instead of AFM order is linked to the itinerancy of $\text{Ru}^{5+} d$ electrons.

To conclude, we have investigated the electronic and magnetic properties of the pyrochlore $(\text{Y}_{1-x}\text{Ca}_x)_2\text{Ru}_2\text{O}_7$, where the substitution of Ca^{+2} at the Y^{3+} site is aimed at producing a mixed valance state of Ru and an insulator-metal transition. No structural transformation is observed with Ca doping up to the substitutional limit of 30%, but lattice parameters are observed to evolve with doping. Magnetic irreversibility and the associated AFM state of the pristine get disrupted with increasing Ca concentration in the lattice. At the higher doping levels, the observation of a hysteric isothermal magnetization curve with a small coercive field indicates a cluster-glasslike transition. The semiconducting behavior of the parent YRO progressively switches over to a bad metallic behavior with Ca doping though the temperature coefficient of resistivity re-

mained negative over all the temperature regimes. The nature of conductivity is found to be Arrhenius type for the parent sample, and it turns out to be 3D-VRH type for the doped samples. The electronic structure calculations for $\text{Y}_2\text{Ru}_2\text{O}_7$ reveal the magnetic structure having an all-out spin arrangement while a spin-glasslike state settles for $(\text{Y}_{1-x}\text{Ca}_x)_2\text{Ru}_2\text{O}_7$, with $x = 0.5$. The DFT results also corroborate the experimental findings on the electronic transport and magnetic properties.

ACKNOWLEDGMENTS

The authors would like to thank HPCE, IIT Madras for providing the computational facility. The author N.M. acknowledges the financial support received from the Department of Science and Technology, India, under the SERB CRG scheme (Ref. No. CRG/2019/004056).

-
- [1] A. Garg, M. Randeria, and N. Trivedi, Strong correlations make high-temperature superconductors robust against disorder, *Nat. Phys.* **4**, 762 (2008).
- [2] N. D. Mathur, F. M. Grosche, S. R. Julian, I. R. Walker, D. M. Freye, R. K. W. Haselwimmer, and G. G. Lonzarich, Magnetically mediated superconductivity in heavy fermion compounds, *Nature (London)* **394**, 39 (1998).
- [3] C. N. R. Rao and A. K. Cheetham, Giant magnetoresistance in transition metal oxides, *Science* **272**, 369 (1996).
- [4] *Colossal Magnetoresistive Oxides*, edited by Y. Tokura (CRC Press, London, 2000).
- [5] E. Dagotto, *Nanoscale Phase Separation and Colossal Magnetoresistance: The Physics of Manganites and Related Compounds*, Springer Series in Solid State Sciences (Springer, Heidelberg, 2003), Vol. 136.
- [6] E. DiMasi, B. Foran, M. C. Aronson, and S. Lee, Stability of charge-density waves under continuous variation of band filling in $\text{LaTe}_{2-x}\text{Sb}_x$ ($0 \leq x \leq 1$), *Phys. Rev. B* **54**, 13587 (1996).
- [7] A. I. Poteryaev, M. Ferrero, A. Georges, and O. Parcollet, Effect of crystal-field splitting and interband hybridization on the metal-insulator transitions of strongly correlated systems, *Phys. Rev. B* **78**, 045115 (2008).
- [8] E. Dagotto, Complexity in strongly correlated electronic systems, *Science* **309**, 257 (2005).
- [9] P. Zubko, S. Gariglio, M. Gabay, P. Ghosez, and J. M. Triscone, Interface physics in complex oxide heterostructures, *Annu. Rev. Condens. Matter Phys.* **2**, 141 (2011).
- [10] Z. Gai, S. V. Kalinin, A. P. Li, J. Shen, and A. P. Baddorf, *In situ* observations and tuning of physical and chemical phenomena on the surfaces of strongly correlated oxides, *Adv. Funct. Mater.* **23**, 2477 (2013).
- [11] R. Schaffer, E. K.-H. Lee, B.-J. Yang, and Y. B. Kim, Recent progress on correlated electron systems with strong spin-orbit coupling, *Rep. Prog. Phys.* **79**, 094504 (2016).
- [12] S. Hameed, J. Joe, D. M. Gautreau, J. W. Freeland, T. Birol, and M. Greven, Two-component electronic phase separation in the doped Mott insulator $\text{Y}_{1-x}\text{Ca}_x\text{TiO}_3$, *Phys. Rev. B* **104**, 045112 (2021).
- [13] A. Oleaga, A. Salazar, M. C. Hatnean, and G. Balakrishnan, Three-dimensional Ising critical behavior in $R_{0.6}\text{Sr}_{0.4}\text{MnO}_3$ ($R = \text{Pr, Nd}$) manganites, *Phys. Rev. B* **92**, 024409 (2015).
- [14] D. Sutter, C. G. Fatuzzo, S. Moser, M. Kim, R. Fittipaldi, A. Vecchione, V. Granata, Y. Sassa, F. Cossalter, G. Gatti *et al.*, Hallmarks of Hund's coupling in the Mott insulator Ca_2RuO_4 , *Nat. Commun.* **8**, 15176 (2017).
- [15] A. Georges, L. De Medici, and J. Mravlje, Strong correlations from Hund's coupling, *Annu. Rev. Condens. Matter Phys.* **4**, 137 (2013).
- [16] R. Kaneko, K. Ueda, C. Terakura, and Y. Tokura, Mott-Hubbard gaps and their doping-induced collapse in strongly correlated pyrochlore ruthenates, *Phys. Rev. B* **102**, 041114(R) (2020).
- [17] T. Munenaka and H. Sato, A novel pyrochlore ruthenate: $\text{Ca}_2\text{Ru}_2\text{O}_7$, *J. Phys. Soc. Japan* **75**, 103801 (2006).
- [18] A. Yamamoto, P. A. Sharma, Y. Okamoto, A. Nakao, H. A. Katori, S. Niitaka, D. Hashizume, and H. Takagi, Metal-insulator transition in a pyrochlore-type ruthenium oxide, $\text{Hg}_2\text{Ru}_2\text{O}_7$, *J. Phys. Soc. Japan* **76**, 43703 (2007).
- [19] R. Kaneko, K. Ueda, S. Sakai, Y. Nomura, M.-T. Huebsch, R. Arita, and Y. Tokura, Fully filling-controlled pyrochlore ruthenates: Emergent ferromagnetic-metal state and geometrical Hall effect, *Phys. Rev. B* **103**, L201111 (2021).
- [20] J. Van Duijn, N. Hur, J. W. Taylor, Y. Qiu, Q. Z. Huang, S.-W. Cheong, C. Broholm, and T. G. Perring, From cooperative paramagnetism to Néel order in $\text{Y}_2\text{Ru}_2\text{O}_7$: Neutron scattering measurements, *Phys. Rev. B* **77**, 020405(R) (2008).
- [21] B. J. Kennedy and IUCr, Structure refinement of $\text{Y}_2\text{Ru}_2\text{O}_7$ by neutron powder diffraction, *Acta Cryst. C* **51**, 790 (1995).
- [22] See Supplemental Material at <http://link.aps.org/supplemental/10.1103/PhysRevB.109.184423> for the Rietveld fit parameters, FE-SEM image, CW fitting, and Arrott plot for Ca-doped $(\text{Y}_{1-x}\text{Ca}_x)_2\text{Ru}_2\text{O}_7$ compositions ranging from $x = 0.0$ to 0.6. Figure S4 illustrates the IRM data for the parent and the 10% Ca-doped sample. Table SII presents the fitting parameters derived from the stretched exponential, logarithmic, and power-law model. Variation of electrical resistivity with temperature for 60% Ca-doped sample is shown in Figs. S6(a) and S6(b).

- Figure S7 depicts the most stable crystal structure of 50% Ca-doped sample. Appendix A of the Supplemental Material includes XRD, magnetic, and IRM data for 40% Ca-doped sample ($Y_{0.6}Ca_{0.4}$) $_2Ru_2O_7$.
- [23] Y. Y. Jiao, J. P. Sun, P. Shahi, Q. Cui, X. H. Yu, Y. Uwatoko, B. S. Wang, J. A. Alonso, H. M. Weng, and J. G. Cheng, Effect of chemical and hydrostatic pressure on the cubic pyrochlore $Cd_2Ru_2O_7$, *Phys. Rev. B* **98**, 075118 (2018).
- [24] R. Kmiec, Z. Świątkowska, J. Gurgul, M. Rams, A. Zarzycki, and K. Tomala, Investigation of the magnetic properties of $Y_2Ru_2O_7$ by ^{99}Ru Mössbauer spectroscopy, *Phys. Rev. B* **74**, 104425 (2006).
- [25] J. Gurgul, M. Rams, Z. Świątkowska, R. Kmiec, and K. Tomala, Bulk magnetic measurements and ^{99}Ru and ^{155}Gd Mössbauer spectroscopies of $Gd_2Ru_2O_7$, *Phys. Rev. B* **75**, 064426 (2007).
- [26] S. Blundell, *Magnetism in Condensed Matter* (Oxford University Press, Oxford, 2001).
- [27] Q. Feng, J. Zou, Y. Wang, Z. Zhao, M. C. Williams, H. Li, and H. Wang, Influence of surface oxygen vacancies and ruthenium valence state on the catalysis of pyrochlore oxides, *ACS Appl. Mater. Interfaces* **12**, 4520 (2020).
- [28] J. Wu, T. Han, and X. Tang, First principle calculations of structural and electronic properties of pyrochlore $Y_2Ru_2O_7$ and $Y_{1-x}M_xRu_2O_{7-\delta}$ ($M = Mg, Ca, Sr, Ba, Zn, Cd$ and Hg), *J. Phys. Chem. Solids* **156**, 110145 (2021).
- [29] G. Berti, S. Sanna, C. Castellano, J. Van Duijn, R. Ruiz-Bustos, L. Bordonali, G. Bussetti, A. Calloni, F. Demartin, L. Duò *et al.*, Observation of mixed valence Ru components in Zn doped $Y_2Ru_2O_7$ pyrochlores, *J. Phys. Chem. C* **120**, 11763 (2016).
- [30] L. Craco, M. S. Laad, S. Leoni, and H. Rosner, Self-doping induced orbital-selective Mott transition in $Hg_2Ru_2O_7$, *Phys. Rev. B* **79**, 075125 (2009).
- [31] S. Baidya and T. Saha-Dasgupta, Covalency driven low-temperature structural distortion and its effect on electronic structure of $Hg_2Ru_2O_7$, *Phys. Rev. B* **91**, 075123 (2015).
- [32] R. Singh, S. K. Srivastava, A. K. Nigam, V. V. Khovaylo, L. K. Varga, and R. Chatterjee, Use of Arrott plots to identify Néel temperature (T_N) in metamagnetic $Ni_{48}Co_6Mn_{26}Al_{20}$ polycrystalline ribbons, *J. Appl. Phys.* **114**, 243911 (2013).
- [33] K. Binder and A. P. Young, Spin glasses: Experimental facts, theoretical concepts, and open questions, *Rev. Mod. Phys.* **58**, 801 (1986).
- [34] J. Ferré, J. Rajchenbach, and H. Maletta, Faraday rotation measurements of time dependent magnetic phenomena in insulating spin glasses (invited), *J. Appl. Phys.* **52**, 1697 (1998).
- [35] K. Katsumata, T. Nire, and M. Tanimoto, Thermoremanent magnetization in $Rb_2Mn_{(1-x)}Cr_xCl_4$ spin-glass, *Solid State Commun.* **43**, 711 (1982).
- [36] A. Kumar, A. Sanger, A. K. Singh, A. Kumar, M. Kumar, and R. Chandra, Experimental evidence of spin glass and exchange bias behavior in sputtered grown α - MnO_2 nanorods, *J. Magn. Magn. Mater.* **433**, 227 (2017).
- [37] P. Tiwari, S. Kumar, and C. Rath, Structural and magnetic phase transitions along with optical properties in $GdMn_{1-x}Fe_xO_3$ perovskite, *J. Appl. Phys.* **126**, 045102 (2019).
- [38] Y. Yeshurun, L. J. P. Ketelsen, and M. B. Salamon, Experimental study of the temperature-field phase diagram of spin-glasses, *Phys. Rev. B* **26**, 1491 (1982).
- [39] S. A. Makhlof, Magnetic properties of Co_3O_4 nanoparticles, *J. Magn. Magn. Mater.* **246**, 184 (2002).
- [40] M. Kumar, R. J. Choudhary, D. K. Shukla, and D. M. Phase, Superspin glassy behaviour of $La_{0.7}Ca_{0.3}Mn_{0.85}Al_{0.15}O_3$ thin film, *J. Appl. Phys.* **116**, 033917 (2014).
- [41] K. Gautam, A. Ahad, S. S. Majid, A. Sagdeo, S. Francoual, R. J. Choudhary, and D. K. Shukla, Deciphering role of the Fe substitution in modulating the structural, magnetic and magnetocaloric properties of $NdCrTiO_5$, *J. Magn. Magn. Mater.* **478**, 260 (2019).
- [42] H. Sompolinsky and A. Zippelius, Dynamic theory of the spin-glass phase, *Phys. Rev. Lett.* **47**, 359 (1981).
- [43] M. D. Mukadam, S. M. Yusuf, P. Sharma, S. K. Kulshreshtha, and G. K. Dey, Dynamics of spin clusters in amorphous Fe_2O_3 , *Phys. Rev. B* **72**, 174408 (2005).
- [44] P. A. Kumar, A. Kumar, K. Kumar, G. A. Babu, P. Vijayakumar, S. Ganesamoorthy, P. Ramasamy, and D. Pandey, Evidence for spin glass transition in hexagonal $DyMnO_3$ without substitutional disorder, *J. Phys. Chem. C* **123**, 30499 (2019).
- [45] S. Sharma, P. Yadav, T. Sau, P. Yanda, P. J. Baker, I. da Silva, A. Sundaresan, and N. P. Lalla, Evidence of a cluster spin-glass state in B-site disordered perovskite $SrTi_{0.5}Mn_{0.5}O_3$, *J. Magn. Magn. Mater.* **492**, 165671 (2019).
- [46] G. Panchal, R. J. Choudhary, M. Kumar, and D. M. Phase, Interfacial spin glass mediated spontaneous exchange bias effect in self-assembled $La_{0.7}Sr_{0.3}MnO_3:NiO$ nanocomposite thin films, *J. Alloys Compd.* **796**, 196 (2019).
- [47] J. Kroder, K. Manna, D. Kriegner, A. S. Sukhanov, E. Liu, H. Borrmann, A. Hoser, J. Gooth, W. Schnelle, D. S. Inosov *et al.*, Spin glass behavior in the disordered half-Heusler compound $IrMnGa$, *Phys. Rev. B* **99**, 174410 (2019).
- [48] A. Kumar, S. D. Kaushik, V. Siruguri, and D. Pandey, Evidence for two spin-glass transitions with magnetoelastic and magnetoelectric couplings in the multiferroic $(Bi_{1-x}Ba_x)(Fe_{1-x}Ti_x)O_3$ System, *Phys. Rev. B* **97**, 104402 (2018).
- [49] R. Hoogerbeets, W.-L. Luo, and R. Orbach, Spin-glass response time in $Ag:Mn$: Exponential temperature dependence, *Phys. Rev. Lett.* **55**, 111 (1985).
- [50] S. R. Dunsiger, R. F. Kiefl, K. H. Chow, B. D. Gaulin, M. J. P. Gingras, J. E. Greedan, A. Keren, K. Kojima, G. M. Luke, and W. A. MacFarlane, Muon spin relaxation investigation of the spin dynamics of geometrically frustrated antiferromagnets $Y_2Mo_2O_7$ and $Tb_2Mo_2O_7$, *Phys. Rev. B* **54**, 9019 (1996).
- [51] V. K. Dwivedi and S. Mukhopadhyay, Coexistence of high electrical conductivity and weak ferromagnetism in Cr doped $Y_2Ir_2O_7$ pyrochlore iridates, *J. Appl. Phys.* **125**, 223901 (2019).
- [52] H. Kumar, R. S. Dhaka, and A. K. Pramanik, Evolution of structure, magnetism, and electronic transport in the doped pyrochlore iridate $Y_2Ir_{2-x}Ru_xO_7$, *Phys. Rev. B* **95**, 054415 (2017).
- [53] Q. Feng, Z. Zhao, X. Z. Yuan, H. Li, and H. Wang, Oxygen vacancy engineering of yttrium ruthenate pyrochlores as an efficient oxygen catalyst for both proton exchange membrane water electrolyzers and rechargeable zinc-air batteries, *Appl. Catal. B Environ.* **260**, 118176 (2020).
- [54] M. Yasukawa, S. Kuniyoshi, and T. Kono, Thermoelectric properties of the $Bi_{1-x}Y_xRu_2O_7$ ($x = 0 - 2$) pyrochlores, *Solid State Commun.* **126**, 213 (2003).
- [55] N. Panwar, I. Coondoo, S. Kumar, S. Kumar, M. Vasundhara, and A. Rao, Structural, electrical, optical and magnetic proper-

- ties of SmCrO_3 chromites: influence of Gd and Mn co-doping, *J. Alloys Compd.* **792**, 1122 (2019).
- [56] N. F. Mott and E. A. Davis, *Electronic Processes in Non-Crystalline Materials* (Oxford University Press, Oxford, 2012).
- [57] N. F. Mott, Conduction in non-crystalline systems: IV. Anderson localization in a disordered lattice, *Philos. Mag.* **22**, 7 (1970).
- [58] G. Kresse and D. Joubert, From ultrasoft pseudopotentials to the projector augmented-wave method, *Phys. Rev. B* **59**, 1758 (1999).
- [59] G. Kresse and J. Furthmüller, Efficient iterative schemes for *ab initio* total-energy calculations using a plane-wave basis set, *Phys. Rev. B* **54**, 11169 (1996).
- [60] S. L. Dudarev, G. A. Botton, S. Y. Savrasov, C. J. Humphreys, and A. P. Sutton, Electron-energy-loss spectra and the structural stability of nickel oxide: An LSDA+*U* study, *Phys. Rev. B* **57**, 1505 (1998).
- [61] S. J. Blundell, T. Lancaster, P. J. Baker, W. Hayes, F. L. Pratt, T. Atake, D. S. Rana, and S. K. Malik, Magnetism and orbitally driven spin-singlet states in Ru oxides: A muon-spin rotation study, *Phys. Rev. B* **77**, 094424 (2008).
- [62] M. A. Subramanian, G. Aravamudan, and G. V. Subba Rao, Oxide pyrochlores—A review, *Prog. Solid State Chem.* **15**, 55 (1983).
- [63] H. Shinaoka, Y. Motome, T. Miyake, and S. Ishibashi, Spin-orbital frustration in molybdenum pyrochlores $A_2\text{Mo}_2\text{O}_7$ (A = rare earth), *Phys. Rev. B* **88**, 174422 (2013).
- [64] M. Miyazaki, R. Kadono, K. H. Satoh, M. Hiraishi, S. Takeshita, A. Koda, A. Yamamoto, and H. Takagi, Magnetic ground state of pyrochlore oxides close to metal-insulator boundary probed by muon spin rotation, *Phys. Rev. B* **82**, 094413 (2010).